



Selective oxidation of methane into formaldehyde and carbon monoxide catalyzed by supported thermally stable iron oxide subnanoclusters prepared from a diiron-introduced polyoxometalate precursor

Keiju Wachi, Tomohiro Yabe^{*}, Takaaki Suzuki, Kentaro Yonesato, Kosuke Suzuki, Kazuya Yamaguchi^{*}

Department of Applied Chemistry, School of Engineering, The University of Tokyo, 7-3-1 Hongo, Bunkyo-ku, Tokyo 113-8656, Japan

ARTICLE INFO

Keywords:

Iron oxide subnanocluster
Polyoxometalate precursor
Methane oxidation
Aggregation inhibition

ABSTRACT

Direct oxidative conversion of methane (CH_4) into useful C1 products remains challenging due to the low reactivity of CH_4 and its facile overoxidation into carbon dioxide (CO_2) under high temperature conditions. Iron oxide (FeO_x) cluster catalysts are promising because of their low activation energy for CH_4 oxidation. However, preliminary results revealed that FeO_x clusters were easily aggregated and deactivated under CH_4 oxidation conditions at 873 K. In this study, we used a diiron-introduced polyoxometalate as a precursor to form thermally stable FeO_x subnanoclusters on SiO_2 , which selectively converted CH_4 into formaldehyde (HCHO) and carbon monoxide (CO) (CH_4 conversion, 2.3%; HCHO and CO selectivity, 87% at 873 K after 1 h). The FeO_x subnanocluster catalyst maintained catalytic activity even after 72 h. Various characterizations, such as STEM, X-ray absorption spectroscopy, and X-ray diffraction, revealed that the *in situ* formed FeO_x subnanoclusters were stabilized by WO_x nanoclusters originating from the polyoxometalate frameworks.

1. Introduction

The recent global increase in the methane (CH_4) supply is primarily attributed to the shale gas revolution. Consequently, catalytic conversion of CH_4 to value-added chemicals has important implications for the efficient use of natural gas resources [1]. To date, CH_4 has been primarily used as an energy source, such as thermal power generation; however, CH_4 combustion gives off carbon dioxide (CO_2). To make effective and environmentally sound use of CH_4 while reducing CO_2 emissions, direct catalytic oxidative conversion of CH_4 into useful C1 products, such as methanol (CH_3OH), formaldehyde (HCHO), and carbon monoxide (CO), is desired [2]. However, the reactivity of CH_4 is quite low due to the significant energy required for its homolytic and heterolytic C–H bond cleavages, and overoxidation into CO_2 can easily proceed under severe conditions that allow for CH_4 activation [3,4]. Therefore, direct and selective oxidation of CH_4 to C1 products without CO_2 emissions is challenging.

Previous studies have focused on metal oxide catalysts at high temperatures (around 873 K). It has been revealed that vanadium- [5], molybdenum- [6], or boron-based [7] oxide catalysts demonstrate

selectivity greater than 80% to C1 products, even at CH_4 conversion higher than 5%. Various iron-based catalysts for CH_4 oxidation have also been reported, such as Fe_2O_3 for chemical looping oxidation of CH_4 [8, 9], an iron dinuclear structure in soluble methane monooxygenase of methane metabolizing enzyme [10], and iron phosphate for the partial oxidation of CH_4 into HCHO and CO [11–14]. In particular, several research groups have reported that nanoparticles or nanoclusters of iron oxide catalysts formed by dispersing a low loading amount of iron precursors on suitable oxide supports, such as mesoporous silica and zeolites, selectively convert CH_4 to HCHO and CO [15–17]. Furthermore, the activation energy of an SiO_2 -supported iron oxide catalyst (102 kJ mol^{-1}) [15] was found to be significantly lower than previously reported activation energies of SiO_2 -supported V_2O_5 , MoO_3 , or CuO_x catalysts (140 – 280 kJ mol^{-1}) [18–20]. These reports indicate that highly dispersed iron oxide species have excellent potential to activate the highly stable C–H bond of CH_4 . However, in general, nanoparticle and nanocluster catalysts are very easily deactivated by aggregation or carbon deposition under high temperature conditions (around 900 K) [21,22]. In fact, in our preliminary examinations, we found that, when an SiO_2 -supported FeO_x nanocluster catalyst prepared with $\text{Fe}(\text{acac})_3$ as

^{*} Corresponding authors.

E-mail addresses: tyabe@g.ecc.u-tokyo.ac.jp (T. Yabe), kyama@appchem.t.u-tokyo.ac.jp (K. Yamaguchi).

<https://doi.org/10.1016/j.apcatb.2022.121420>

Received 17 January 2022; Received in revised form 30 March 2022; Accepted 14 April 2022

Available online 19 May 2022

0926-3373/© 2022 Elsevier B.V. All rights reserved.

a precursor was used for CH₄ oxidation at 873 K for 24 h, the FeO_x nanoclusters formed at the early stage of the reaction gradually aggregated, causing catalyst deactivation (see Fig. 1 and Section 3, Results and discussion). Therefore, FeO_x clusters that remain stable under high temperature reaction conditions are required. In the case of CH₄ oxidation using supported nanoparticle catalysts under high temperature conditions, it has been reported that aggregation and carbon deposition can be suppressed by covering the nanoparticle surface with another metal oxides to form core-shell structures [23–25]. However, few studies have investigated core-shell structures of nanoclusters that are smaller than nanoparticles [26,27]; most reported nanoclusters were stabilized by covering them with organic ligands. However, maintaining the cluster size under high temperature reaction conditions where the ligands undergo thermal decomposition is extremely difficult [28]. Therefore, a new catalyst design strategy that can stably retain active nanoclusters even at high temperatures is required.

A polyoxometalate (POM) is an anionic metal oxide cluster consisting of metal-oxygen polyhedral units, such as {WO₆} [29,30]. The structure formed by eliminating some of the polyhedral units is called a lacunary POM, which functions as an inorganic multidentate ligand and allows the introduction of different metals [31–33]. Recently, we reported a new synthesis method to introduce various multinuclear metal oxide clusters into lacunary POMs in organic solvents [34–37]. Pei et al. previously investigated CH₄ oxidation activity over various POM-based catalysts, such as [XY₁₂O₄₀]ⁿ⁻ and [XMY₁₁O₄₀]^{m-} (X = Si or P, Y = W or Mo, M = 3d metals) supported on mesoporous silica [38–40]. However, catalytic activities of multinuclear metal-introduced POMs have not been investigated in gas-phase reactions at high temperature. In the

multinuclear metal-introduced POMs, metal oxide clusters are surrounded by rigid frameworks of lacunary POMs. POMs, such as H₄SiW₁₂O₄₀, are known to decompose into SiO₂ and WO₃ above 799 K [41]. Therefore, unlike organic ligands, which are easily burned out, rigid inorganic ligands are expected to inhibit the aggregation of internal metal oxide clusters even under high temperature oxidation conditions.

According to the above consideration, we have used a POM with an iron dinuclear core (Fe₂) as a precursor and constructed highly stable FeO_x subnanoclusters that selectively converted CH₄ into HCHO and CO (Fig. 1). The *in situ* formed FeO_x subnanocluster catalyst derived from Fe₂ maintained its catalytic activity for 72 h under CH₄ oxidation conditions at 873 K.

2. Experimental

2.1. Catalyst characterization

Cold-spray ionization (CSI)-mass spectra were recorded on a JEOL JMS-T100CS. Infrared (IR) spectra were measured on a Jasco FT/IR-4100 using KBr disks. Inductively coupled plasma atomic emission spectroscopy analyses for Si, Fe, and W were performed on a Shimadzu ICPS-8100. Elemental analyses for C, H, and N were performed on Elementar vario MICRO cube at the Elemental Analysis Centre of the School of Science of the University of Tokyo. The single-crystal X-ray diffraction (XRD) experiment was performed on a Rigaku XtaLAB Synergy-R diffractometer with a HyPix-6000HE detector and a rotating anode Mo K α radiation (λ = 0.71073 Å, 50 kV, 24 mA) at 93 K. CrysAlisPro

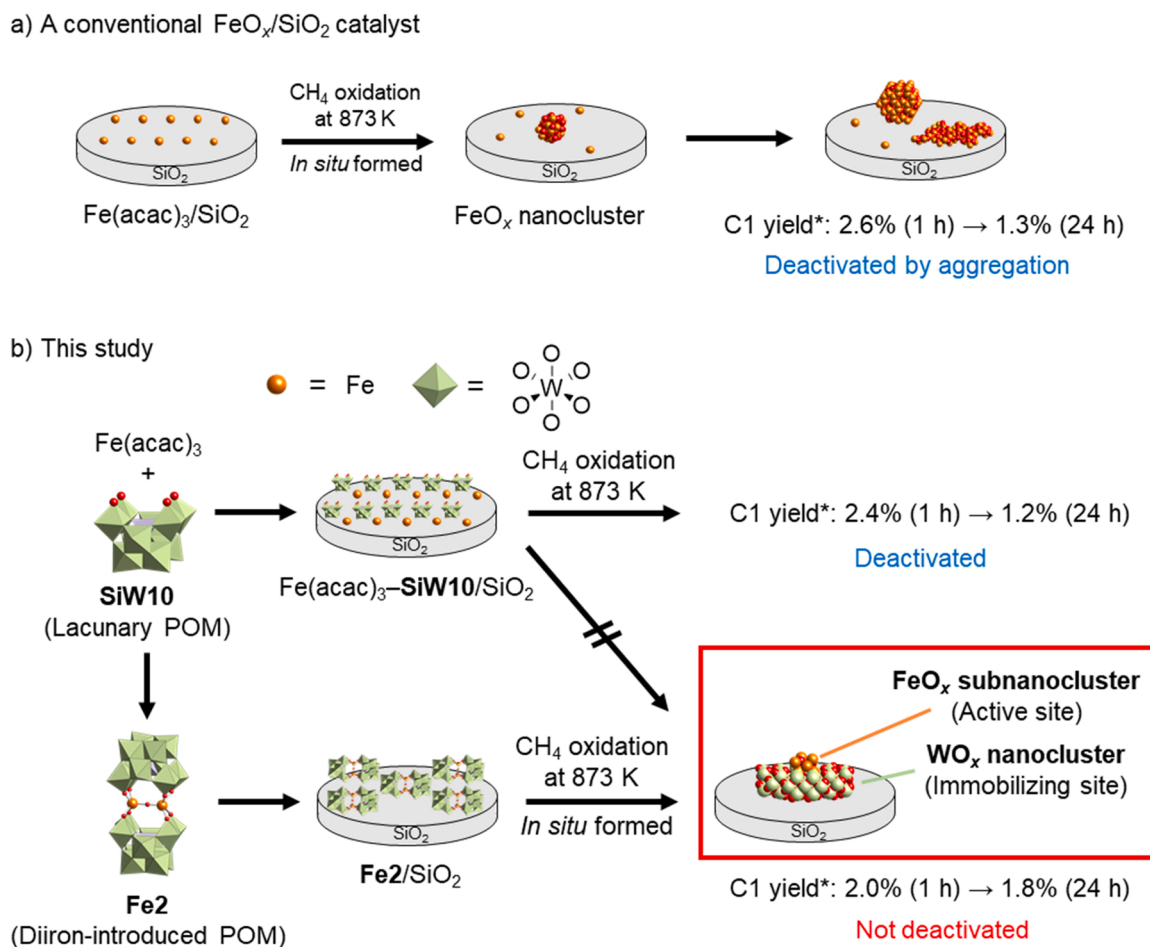


Fig. 1. Schematic diagram of catalytic performance for CH₄ oxidation over (a) a conventional SiO₂-supported iron oxide (FeO_x) nanocluster catalyst and (b) the *in situ* formed FeO_x subnanocluster catalyst using Fe₂ as a precursor (this study). *C1 yield is the total of HCHO and CO yields.

software was used to collect and process data [42]. In the reduction of data, Lorentz and polarization corrections were made. The structure of **Fe2** was solved by SHELXS-2013/1 (direct methods) and refined by SHELXL-2018/3 [43,44]. Non-hydrogen atoms were refined as anisotropic. The SQUEEZE program [45] was used to omit the highly disordered tetra-*n*-butylammonium (TBA) cations and solvent molecules. Powder XRD patterns were measured using a Rigaku SmartLab high-resolution X-ray diffractometer (Cu K α , λ = 1.5405 Å, 45 kV, 200 mA). Brunauer–Emmett–Teller (BET) surface areas were measured by N₂ adsorption at 77 K using a Micromeritics ASAP 2010 instrument. Raman spectra were recorded on a JASCO NRS-5100 spectrometer. The measurement conditions included an irradiation laser wavelength of 532 nm, a laser power at 10.2 mW. The data were collected twice with a measurement time of 3 min. High-angle annular dark-field scanning transmission electron microscopy (HAADF-STEM) analyses were performed on a JEOL JEM-ARM200F instrument equipped with energy-dispersive X-ray spectrometry (EDS) at 200 kV. X-ray absorption spectroscopy (XAS) of the Fe K-edge and W L₃-edge was carried out using the transmission and fluorescence method at the BL14B2 beamline of Spring-8. The X-ray beam was monochromatized using an Si (111) monochromator for the Fe K-edge XAS and an Si (311) crystal monochromator for the W L₃-edge XAS. The energy was calibrated by using an Fe metal foil for the Fe K-edge XAS and a W metal foil for the W L₃-edge XAS. X-ray absorption near-edge structure (XANES) and extended X-ray absorption fine structure (EXAFS) data were analyzed by using Athena and Artemis software (Demeter, ver. 0.9.26; Bruce Ravel). The k^3 -weighted EXAFS spectra were Fourier-transformed into R -space in the range of 3–12 Å^{−1} for Fe and 3–13 Å^{−1} for W. The XAS measurement methods and EXAFS analyses are explained in detail in the [Supporting Information](#).

2.2. Synthesis of **Fe2**

Acetone, acetonitrile, dichloroethane, and ethyl acetate used as solvents were purchased from Kanto Chemicals. Iron(III) acetylacetonate (Fe(acac)₃), the introduced metal precursor for **Fe2**, was purchased from Sigma-Aldrich. TBA₄[H₄(γ -SiW₁₀O₃₆)·H₂O (**SiW10**) was synthesized according to the reported procedures [46,47]. To an acetone solution (40 mL) of Fe(acac)₃ (103 mg, 291 μ mol), **SiW10** (1.00 g, 291 μ mol) was added. The resulting solution was stirred for 24 h at room temperature. The generated precipitate was collected by filtration through a membrane filter. After vacuum drying, a powder sample of **Fe2** was obtained (42% yield based on **SiW10**). Light orange single crystals suitable for X-ray crystallographic analysis were obtained by recrystallization from a mixture solution of acetonitrile, dichloroethane, and ethyl acetate. The anionic structure of **Fe2** was determined by X-ray crystallographic analysis, in which the Fe–O–Fe core is sandwiched by two [γ -SiW₁₀O₃₆]^{8−} units (Fig. S1 and Table S1). IR (KBr pellet, cm^{−1}): 3455, 2961, 2873, 1634, 1484, 1382, 1107, 1058, 1026, 997, 958, 892, 793, 719, 551, 396, 359, 319, 308. Elemental analysis: calcd (%) for TBA₄H₄[Fe₂O(SiW₁₀O₃₆)₂], H 4.20, C 22.10, N 1.61, Si 0.81, Fe 1.61, W 52.86; found H 4.31, C 21.88, N 1.63, Si 0.79, Fe 1.57, W 52.46. Positive-ion CSI-mass (acetonitrile): m/z = 7198.56, [TBA₄H₄Fe₂O(SiW₁₀O₃₆)₂]⁺ (theoretical m/z = 7198.86) (Fig. S2).

2.3. Preparation of **Fe2**/SiO₂

The BET surface area of **Fe2** powder was calculated at 2.45 m² g^{−1} by N₂ adsorption. A low BET surface area was likely to cause low accessibility of CH₄. Therefore, **Fe2** was dispersed on SiO₂ with high specific surface area (CARIAC Q-10 supplied by Fuji Silysia Chemical Ltd, 300 m² g^{−1}) using the incipient wetness method. First, **Fe2** powder (100 mg) was dissolved in acetonitrile (2 mL). Then, the resulting solution was dropped onto a thin layer of SiO₂ (900 mg) spread on an evaporation tray. The resulting orange powder was dried at 373 K for 5 h under air atmosphere to obtain **Fe2**/SiO₂. High dispersion of **Fe2**

was confirmed by XRD; **Fe2** diffraction peaks in 5–8 degrees disappeared after supporting on SiO₂ (Fig. S3). Furthermore, Fe K-edge EXAFS spectra of **Fe2** and **Fe2**/SiO₂ could be reproduced using Fe–O shells derived from **Fe2**. (Figs. S4 and S5). Fe(acac)₃/SiO₂, **SiW10**/SiO₂, and Fe(acac)₃-**SiW10**/SiO₂, which was supported on SiO₂ by stepwise addition of Fe(acac)₃ and **SiW10** in acetonitrile, were prepared using a method similar to that of **Fe2**/SiO₂. To accurately compare the catalytic properties per Fe content, various SiO₂-supported Fe catalysts were prepared with Fe loading amounts of 0.16 wt%. As for Fe(acac)₃ precursor, the catalyst with Fe loading amounts of 1.6 wt% (named as 10Fe(acac)₃/SiO₂) was also prepared to investigate the effect of high dispersion of Fe species.

2.4. Evaluation of CH₄ oxidation activity

Catalytic activity tests for CH₄ oxidation were conducted using a fixed bed flow-type reactor. A schematic image of the reactor is shown in Fig. S6. After 100 mg catalyst was charged into the quartz tube reactor (6.0 mm i.d.), the reactant gas (CH₄:O₂:Ar = 2:1:7, total flow rate: 50 mL min^{−1}) was fed into the reactor. Then, the input temperature of the tube furnace charged with the catalyst was elevated to 873 K at a rate of 10 K min^{−1}. The inlet and outlet gas were heated at 373 K to reduce the temperature distribution in the catalyst bed and to suppress the condensation of products. When the furnace temperature reached 873 K, that temperature was maintained for 1 h to combust the CO₂ derived from the organic components of the catalyst precursor, such as TBA cations, and to eliminate the effect on the quantitative evaluation of CO and CO₂. Pretreatment with different gas atmospheres did not affect the catalytic activity of **Fe2**/SiO₂ (Table S2). After the calcination for 1 h, the product gases were analyzed using the Nexis GC-2030 with a barrier discharge ionization detector (Shimadzu Corporation) with a SHINCARBON ST packed column and a gas chromatograph-mass spectrometer (GC-MS QP-2010 Ultra; Shimadzu Corporation) with a Rt-Q-Bond capillary column at an ionization voltage of 70 eV. A trace amount of methanol was detected by the GC-MS analysis. The respective calculation formulas for CH₄ conversion, product selectivity, and product yield in this study are as follows.

$$\text{CH}_4 \text{ conversion (\%)} = \frac{\text{Total carbon moles of HCHO, CO, and CO}_2}{\text{Carbon moles of input CH}_4} \times 100$$

$$\text{Product selectivity (\%)} = \frac{\text{A carbon mole of HCHO, CO, or CO}_2}{\text{Total carbon moles of HCHO, CO, and CO}_2} \times 100$$

$$\text{Product yield (\%)} = \text{CH}_4 \text{ conversion (\%)} \times \text{Product selectivity (\%)} \div 100$$

3. Results and discussion

3.1. Evaluation of CH₄ oxidation activity

Firstly, the catalytic property of **Fe2**/SiO₂ was investigated under several conditions. CH₄ conversion was 2.3% under the standard condition (total flow rate: 50 mL min^{−1}, CH₄:O₂:Ar = 2:1:7, 873 K, 1 atm), and the selectivities to HCHO and CO were 41% and 46%, respectively (Table 1, Entry 1). Selectivity to CO₂, an undesirable byproduct, was only 13%. Fig. S7 shows the effect of contact time (W/F) on CH₄ conversion and C1 products selectivity. As CH₄ conversion was increased by increasing contact time, HCHO selectivity decreased, while CO selectivity increased. Although CO₂ selectivity slightly increased as well, it remained as low as 16% even at high CH₄ conversion of 5.1%. As a result, C1 products (HCHO and CO) total yield over **Fe2**/SiO₂ was higher than any other previously reported iron-based catalysts (4.3%), indicating that complete oxidation of CH₄ was highly suppressed over **Fe2**/SiO₂ (Table S3) [11–14].

To compare the reaction mechanism to previously reported iron-

Table 1CH₄ oxidation catalyzed by various Fe-based catalysts [a].

Entry	Catalyst	Fe [wt%]	Conv. [%]	Sel. [%]			Yield [%]	TOF
				CH ₄	HCHO	CO		
1	Fe2 /SiO ₂	0.16	2.3	41	46	13	2.0	2.2 × 10 ²
2	Fe2	1.6	0.56	31	35	34	0.4	5.3
3 ^[b]	Fe ₂ O ₃	70	5.9	n.d.	n.d.	100	–	1.3
4	SiW10 /SiO ₂	–	0.22	73	19	8	0.2	–
5 ^[c]	Fe(acac) ₃ /SiO ₂	0.16	3.5	36	37	27	2.6	6.6 × 10 ²
6 ^[c,d]	Fe2 /SiO ₂	0.16	3.2	44	47	9	2.9	1.2 × 10 ²
7 ^[c,e]	10Fe(acac) ₃ /SiO ₂	1.6	2.1	11	38	51	1.0	39
8	Fe(acac) ₃ - SiW10 /SiO ₂	0.16	2.8	24	62	15	2.4	2.7 × 10 ²

[a] Reaction conditions: catalyst (100 mg), CH₄:O₂:Ar = 2:1:7, 50 mL min⁻¹, 873 K, 1 atm, 1 h. [b] 673 K. [c] 100 mL min⁻¹. [d] Catalyst (500 mg). [e] Catalyst (50 mg).

based catalysts, reaction kinetic studies over **Fe2**/SiO₂ were also performed. First, the effect of partial pressures of CH₄ and O₂ on the CH₄ conversion rate was investigated at 873 K (Fig. S8). The reaction order with respect to CH₄ was 0.71, while the reaction order with respect to O₂ was 0.33. No oxygen pressure dependence was observed over iron phosphate or vanadium oxide catalysts which follow Mars–van Krevelen (MvK) mechanism [11,18]. In fact, SiO₂-supported iron oxide catalysts have been reported not to follow the MvK mechanism [15], and the pressure dependences on the reaction using **Fe2**/SiO₂ were similar to those using the reported SiO₂-supported iron oxide catalysts, indicating that FeO_x cluster were formed over **Fe2**/SiO₂. Next, the temperature dependence of the CH₄ conversion rate was investigated between 823 K and 923 K (Fig. S9). The apparent activation energy calculated from the Arrhenius plot was 92.6 kJ mol⁻¹. The activation energies for CH₄ oxidation of previously reported iron-based catalysts are significantly lower (102–126 kJ mol⁻¹) than previously reported activation energies of vanadium- (227–281 kJ mol⁻¹) or molybdenum-based (189 kJ mol⁻¹) catalysts; however, the activation energy over **Fe2**/SiO₂ was even lower than those over any other iron-based catalysts (Table S4) [11,15,18,19,48].

Next, initial catalytic activity for CH₄ oxidation was investigated over various Fe and POM catalysts at 873 K under atmospheric pressure. The results are summarized in Table 1. The unsupported **Fe2** catalyst had a significantly lower CH₄ conversion than that of **Fe2**/SiO₂ (Table 1, Entry 2). The XRD pattern of unsupported **Fe2** after 5 h reaction exhibited diffraction peaks due to WO₃, suggesting that bulk WO₃ derived from **Fe2** decomposition covered the FeO_x nanocluster surface and hindered substrate access (Fig. S3). On the other hand, diffraction peaks for Fe₂O₃ or WO₃ did not appear in the XRD pattern of **Fe2**/SiO₂ even after 24 h reaction (Fig. S3), indicating that the highly dispersed FeO_x cluster on SiO₂ enabled highly efficient substrate access. The bulk Fe₂O₃ catalyst showed high CH₄ conversion even at a relatively low temperature of 673 K; however, only CO₂ was produced (Table 1, Entry 3). It is known that CH₄ oxidation over bulk Fe₂O₃ also follows MvK mechanism as well as other metal oxide [49], and that overoxidation into CO₂ is kinetically more favorable due to the high nucleophilicity of the lattice oxygen in Fe₂O₃ [7]. It has previously been reported that a tungsten-based POM catalyst was inactive for CH₄ oxidation [50]. The CH₄ conversion with **SiW10**/SiO₂ was only 0.22% (Table 1, Entry 4). These results indicate that neither bulk iron oxide nor tungsten oxide species derived from **SiW10** frameworks were the active species for the present CH₄ oxidation.

Selective oxidation of CH₄ also proceeded over Fe(acac)₃/SiO₂, with 73% selectivity to the desired C1 products (HCHO and CO) at 3.5% CH₄ conversion (Table 1, Entry 5). This catalytic performance was in good agreement with that over a previously reported FeO_x/SiO₂ catalyst prepared by a sol-gel method [16]. Compared to **Fe2**/SiO₂, CH₄ conversion rate over Fe(acac)₃/SiO₂ was higher, but the selectivity to C1 products was lower at the same CH₄ conversion (Table 1, Entries 5 and 6). Furthermore, when the loading amount of Fe(acac)₃ was increased to

10 wt%, the selectivity to undesirable CO₂ was greater than 50%, even at lower CH₄ conversion of 2.1% (Table 1, Entry 7). This was probably because, as the iron content in the SiO₂-supported iron catalyst increased, larger iron oxide particles were formed under the reaction conditions, demonstrating activities similar to that of the bulk Fe₂O₃ catalyst. Therefore, it was elucidated that highly selective conversion of CH₄ to HCHO and CO proceeded on the *in situ* formed FeO_x nanoclusters during the reaction on the catalysts with low Fe loading amounts. In addition, Fe(acac)₃-**SiW10**/SiO₂ showed high C1 products selectivity as well as **Fe2**/SiO₂ (Table 1, Entry 8). Finally, not only the selectivities to C1 products but also the turnover frequency (TOF) values in the catalysts with low amounts of iron loading (Table 1, Entries 1, 5, and 8) was much higher than those of the catalysts with high amounts of iron loading (Table 1, Entries 2 and 7). Thus, highly dispersed FeO_x nanoclusters are responsible for high yield of C1 products.

Next, 24 h CH₄ oxidation tests were conducted over three catalysts, **Fe2**/SiO₂, Fe(acac)₃/SiO₂, and Fe(acac)₃-**SiW10**/SiO₂, that showed high C1 yield in the above control experiments. **Fe2**/SiO₂ maintained catalytic performance even after 24 h, demonstrating 1.9% CH₄ conversion and 91% C1 products selectivity (Fig. 2a). Furthermore, neither significant decrease in CH₄ conversion nor change in C1 products selectivity was observed when the reaction time was extended to 72 h (Fig. S10). On the other hand, with Fe(acac)₃/SiO₂, CH₄ conversion decreased significantly over time, while C1 products selectivity was increased slightly (Fig. 2b). As a result, C1 yield decreased from 2.6% after 1 h to 1.3% after 24 h, indicating that FeO_x nanoclusters in Fe(acac)₃/SiO₂ deactivated over time at 873 K. Fe(acac)₃-**SiW10**/SiO₂ showed a similar tendency to Fe(acac)₃/SiO₂; C1 yield decreased from 2.4% after 1 h to 1.2% after 24 h (Fig. 2c). These results suggest that the *in situ* formed FeO_x nanoclusters on SiO₂ could be maintained even at 873 K only when **Fe2** was used as a precursor, i.e., when the iron dimeric structure was introduced into the rigid POM template in advance.

3.2. Characterization of Fe(acac)₃/SiO₂ after CH₄ oxidation

Fe K-edge XAFS analysis was performed on Fe(acac)₃/SiO₂ after CH₄ oxidation to confirm the formation of FeO_x clusters from the Fe(acac)₃ precursor. The Fe–O region of 1.0–2.1 Å in the EXAFS spectrum of Fe(acac)₃/SiO₂ could be reproduced by using an Fe–O shell derived from Fe₂O₃ (Fig. S11). The low coordination number (CN) of 2.5 supports the formation of FeO_x nanoclusters from Fe(acac)₃ precursors under the CH₄ oxidation conditions.

Next, we investigated the reason why Fe(acac)₃/SiO₂ was deactivated. Firstly, in the Raman spectra of Fe(acac)₃/SiO₂ and **Fe2**/SiO₂ after 24 h reaction, no peak derived from G-band or D-band of graphitic carbon was observed, indicating that carbon deposition was not a main reason for the deactivation of Fe(acac)₃/SiO₂ (Fig. S12). Then, we observed the change in the particle size of the *in situ* formed FeO_x clusters by HAADF-STEM (Fig. 3). In the HAADF-STEM image of Fe(acac)₃/SiO₂ after 5 h reaction, single atom like species and FeO_x

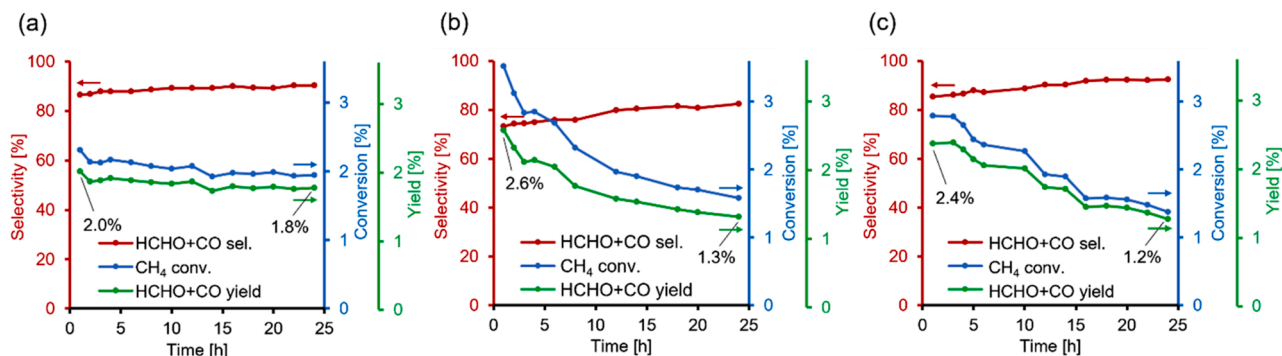


Fig. 2. Time course examination for CH₄ oxidation for 24 h over (a) Fe₂/SiO₂, (b) Fe(acac)₃/SiO₂, and (c) Fe(acac)₃-SiW10/SiO₂. The reaction conditions were the same as Table 1.

nanoclusters with a particle size of approximately 1 nm were observed (Figs. 3a and S13a). As for Fe(acac)₃/SiO₂ after 24 h reaction, single atom species still remained while the average size of FeO_x nanoclusters was increased to approximately 2 nm (Figs. 3b and S13b). Furthermore, another type of FeO_x species spread on the surface of SiO₂ was also observed on Fe(acac)₃/SiO₂ after 24 h reaction, although such island-like Fe species were not observed on Fe(acac)₃/SiO₂ after 5 h reaction (Fig. 3c). The size of this island-like Fe species was obviously larger than the FeO_x nanoclusters. These data indicate that FeO_x nanoclusters were aggregated over time under CH₄ oxidation conditions at 873 K. It is well known that iron oxide on the support exhibits a low tendency to sintering among 3d metals [51]. However, in this study, we revealed that FeO_x nanoclusters formed on SiO₂ using Fe(acac)₃ as a precursor aggregated at 873 K even at low Fe loading (0.16 wt%) and that the aggregation caused significant deactivation.

3.3. Characterization of the Fe₂/SiO₂ after CH₄ oxidation

To investigate the thermally stable active species in Fe₂/SiO₂, we analyzed the *in situ* formed iron oxide and tungsten oxide species on Fe₂/SiO₂ after CH₄ oxidation using Fe K-edge and W L₃-edge XAS and STEM. The W L₃-edge EXAFS spectrum of Fe₂/SiO₂ after 5 h reaction changed from the spectrum of unsupported Fe₂ and could be reproduced by using a W-O shell derived from WO₃ (Figs. 4a, S14, and S15). This result indicated that SiW10 frameworks were decomposed into WO_x species during the CH₄ oxidation conditions at 873 K. Furthermore, there was no WO₃ peak in the XRD patterns of Fe₂/SiO₂ after 24 h reaction, indicating that no bulk WO₃ particles were formed (Fig. S3). Actually, nanoclusters of approximately 3 nm were observed in the

HAADF-STEM image of Fe₂/SiO₂ after 24 h reaction (Fig. 4b). Iron could not be distinguished from tungsten due to the extremely low loading amount of iron (0.16 wt%, i.e., one-tenth of tungsten loading). On the other hand, the STEM-EDS mapping showed that iron and tungsten atoms were located in almost the same region (Fig. 4c and d). Thus, after the decomposition of the Fe₂ precursor, iron oxide species were possibly highly dispersed on WO_x nanoclusters.

The detailed structure of the *in situ* formed iron oxide species in Fe₂/SiO₂ was elucidated by Fe K-edge XAS analysis. Fig. 4e shows the Fe K-edge XANES spectra of Fe₂O₃, unsupported Fe₂, Fe₂/SiO₂ after 5 h reaction, Fe(acac)₃, and Fe(acac)₃/SiO₂ after 5 h reaction. The absorption edge energy of each sample is close to that of Fe₂O₃, indicating that the valence state of Fe in all samples is +3. After 5 h reaction, three possible Fe₂/SiO₂ structures are formed after decomposition. The first is an Fe-O-Fe structure in the remaining Fe₂ precursor even though SiW10 frameworks were decomposed. The second is a composite oxide of iron and tungsten, such as Fe₂WO₆ or Fe₂(WO₄)₃. The third is an FeO_x cluster dispersed on a WO_x nanocluster. Firstly, the white line intensity of Fe₂/SiO₂ after 5 h reaction decreased compared to that of Fe₂ precursor, and the white line feature is also different from bulk Fe₂O₃, shown in Fig. 4e. In addition, the shape of the EXAFS spectrum of Fe₂/SiO₂ after 5 h reaction differed from those of Fe₂ precursor and bulk Fe₂O₃, shown in Figs. 4f and S16. Similarly, the white line intensity of Fe(acac)₃/SiO₂ after 5 h reaction, which formed FeO_x nanoclusters by the decomposition of Fe(acac)₃ precursor, decreased compared to that of Fe(acac)₃ precursor, and the white line feature is also different from bulk Fe₂O₃, shown in Fig. 4e. In addition, the shape of the EXAFS spectrum of Fe(acac)₃/SiO₂ after 5 h reaction differed from those of Fe(acac)₃ precursor and bulk Fe₂O₃, shown in Figs. 4f and S16. Thus, these results

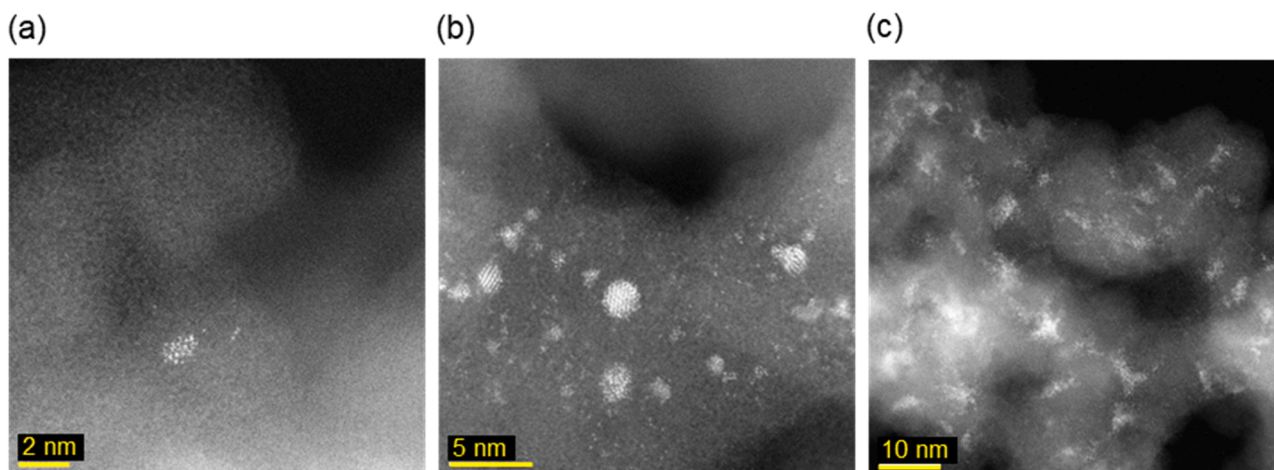


Fig. 3. HAADF-STEM images of Fe(acac)₃/SiO₂ after CH₄ oxidation. (a) after 5 h and (b, c) after 24 h.

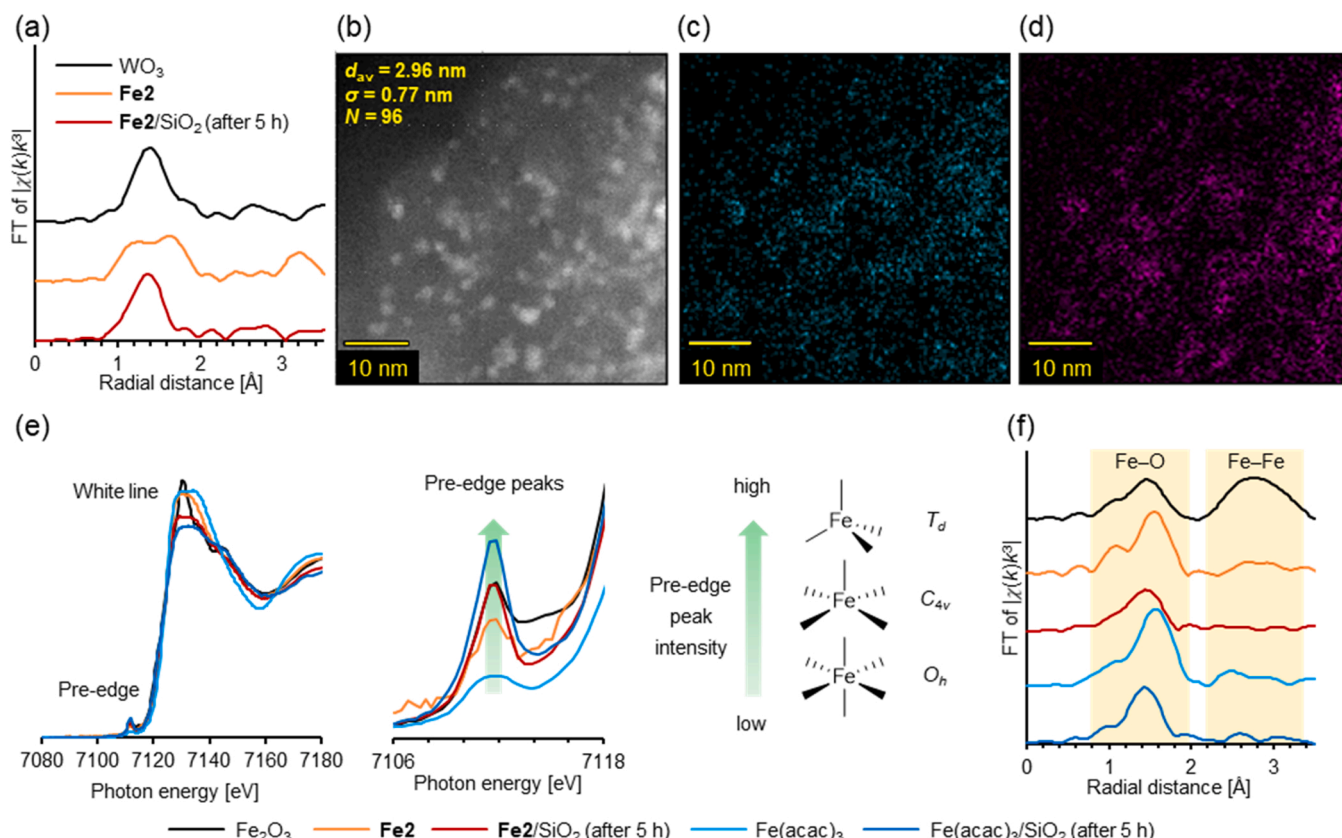


Fig. 4. Characterization of the **Fe2/SiO2** after CH_4 oxidation. (a) k^3 -weighted Fourier-transformed W L_3 -edge EXAFS spectra; (b) HAADF-STEM image of **Fe2/SiO2** (after 24 h); (c, d) STEM-EDS mappings, showing distributions of Fe in cyan (panel (c)) and W in magenta (panel (d)) of **Fe2/SiO2** (after 24 h); (e) Fe K-edge XANES spectra and magnification of pre-edge region; (f) k^3 -weighted Fourier-transformed Fe K-edge EXAFS spectra.

indicate that the dimeric Fe–O–Fe structure in the initial **Fe2** structure was decomposed as well as the W species. Furthermore, the pre-edge feature in the XANES spectra negated the formation of the composite oxide. In the Fe K-edge XANES spectra, pre-edge peaks derived from $1s \rightarrow 3d$ transitions can be observed; however, the peaks are weak because $1s \rightarrow 3d$ transitions are forbidden by parity selection rules. It has been reported that the pre-edge peak intensity significantly depends on the coordination geometry of Fe species because the hybridization of the 4p and 3d orbitals allows for properties similar to those of the $1s \rightarrow 4p$ transition [52]. In general, the pre-edge peak intensity decreases in the following order: tetragonal (T_d) < square pyramidal (C_{4v}) < octahedral (O_h) symmetry. As shown in Fig. 4e, the pre-edge peak intensity of **Fe2/SiO2** after 5 h reaction was much higher than unsupported **Fe2** in which Fe species have a distorted C_{4v} symmetry. On the other hand, the pre-edge peak intensity of the composite oxide species, such as Fe_2WO_6 and $\text{Fe}_2(\text{WO}_4)_3$, is typically much lower than unsupported **Fe2** and close to that of $\text{Fe}(\text{acac})_3$ due to O_h symmetry. Therefore, the most reasonable model is that iron oxide clusters are dispersed on WO_x clusters. In fact, the EXAFS spectrum of **Fe2/SiO2** after 5 h reaction could be reproduced by using an Fe–O shell derived from Fe_2O_3 , supporting the formation of FeO_x cluster species in **Fe2/SiO2** (Fig. S14). In addition, there was no peak in the Fe–Fe region around 2.6 Å in the EXAFS spectrum of **Fe2/SiO2** after 5 h reaction although bulk Fe_2O_3 has a large peak in that region, as shown in Fig. 4f. In a previous report on FeO_x subnanoclusters smaller than 1 nm, an Fe–Fe peak around 2.6 Å was hardly observed in the Fe K-edge EXAFS spectrum [53]. Thus, the *in situ* formed FeO_x clusters in **Fe2/SiO2** were subnanometric size. Furthermore, the following two evidence supports the existence of the interaction between FeO_x and WO_x species. Comparing inverse Fourier transforms of Fe K-edge EXAFS spectra for the first coordinated shell ($R = 1.0$ – 2.1 Å), the spectra of Fe_2O_3 and $\text{Fe}(\text{acac})_3/\text{SiO}_2$ after the reaction are different

from those of **Fe2/SiO2** before and after the reaction, suggesting that there is an interaction between FeO_x and WO_x , as shown in Fig. S17. Another evidence is the localization of Fe and W species in the same region in EDS mapping, as shown in Fig. 4c and d.

From the above discussions, we concluded that FeO_x subnanoclusters formed under the given reaction conditions were dispersed on WO_x nanoclusters originated from the **SiW10** frameworks, which suppressed the aggregation of the FeO_x subnanoclusters and maintained catalytic activity even after 72 h. Furthermore, the deactivation over time in $\text{Fe}(\text{acac})_3$ -**SiW10**/ SiO_2 suggests that using **Fe2** as a precursor played a key role in the suppression of FeO_x cluster aggregation.

4. Conclusion

The catalyst with a diiron-introduced polyoxometalate (**Fe2**) precursor dispersed on SiO_2 (**Fe2/SiO2**) exhibited high selectivity of 87% into C1 products (HCHO and CO) at 2.3% CH_4 conversion at 873 K after 1 h under ambient pressure. **Fe2/SiO2** exhibited much higher selectivities to HCHO and CO compared to conventional FeO_x cluster catalysts at the same CH_4 conversion. Furthermore, $\text{Fe}(\text{acac})_3/\text{SiO}_2$ deactivated after 24 h due to the aggregation of FeO_x cluster active sites, while **Fe2/SiO2** maintained the catalytic activity even after 72 h. Fe K-edge XAFS, W L_3 -edge XAFS, and HAADF-STEM analyses revealed that **Fe2** precursor was decomposed into FeO_x subnanocluster and WO_x nanocluster under CH_4 oxidation conditions at 873 K. In addition, STEM-EDS mapping demonstrated that FeO_x subnanoclusters were dispersed on WO_x nanoclusters. Thus, the lifetime of the **Fe2/SiO2** in CH_4 oxidation at 873 K was extended since WO_x species suppressed the aggregation of FeO_x subnanoclusters, and its protective effect was achieved by the introduction of iron atoms into the lacunary polyoxometalate in advance. In future, the strategy to employ a metal-introduced POM as a

precursor to form thermally stable metal oxide clusters is expected to be applied to other catalytic gas-phase reactions performed at high temperature.

CRediT authorship contribution statement

K. Wachi: Conceptualization, Data curation, Formal analysis, Investigation, Methodology, Visualization, Writing – original draft, Writing – review & editing. **T. Yabe:** Conceptualization, Data curation, Formal analysis, Funding acquisition, Investigation, Methodology, Project administration, Resources, Supervision, Visualization, Writing – original draft, Writing – review & editing. **T. Suzuki:** Conceptualization, Data curation, Investigation, Methodology, Visualization, Writing – review & editing. **K. Yonesato:** Data curation, Investigation, Methodology, Visualization, Writing – original draft, Writing – review & editing. **K. Suzuki:** Conceptualization, Data curation, Methodology, Resources, Supervisions, Writing – review & editing. **K. Yamaguchi:** Conceptualization, Data curation, Funding acquisition, Methodology, Project administration, Resources, Supervision, Visualization, Writing – review & editing.

Declaration of Competing Interest

The authors declare that they have no known competing financial interests or personal relationships that could have appeared to influence the work reported in this paper.

Acknowledgments

This work was financially supported by Japan Society for the Promotion of Science (JSPS) KAKENHI, Japan, Grant Number 20K15085 and The Japan Science and Technology Agency, Core Research for Evolutionary Science and Technology (JST CREST), Japan, Grant Number JPMJCR17P4. A part of this work was supported by the “Grant for Research” of The Japan Petroleum Institute and Mizuho Foundation for the Promotion of Sciences. A part of this work was conducted at the Advanced Characterization Nanotechnology Platform of the University of Tokyo, supported by “Nanotechnology Platform” of the Ministry of Education, Culture, Sports, Science and Technology (MEXT), Japan, Grant Number JPMXP09A21UT0199. We thank Mr. Hiroyuki Oshikawa and Ms. Mari Morita in Institute of Engineering Innovation for the STEM measurements. We greatly appreciate Dr. Hironori Ofuchi (Japan Synchrotron Radiation Research Institute, SPring-8) for the support of XAFS measurements at BL14B2, Proposal Number 2021A1620.

Appendix A. Supporting information

Supplementary data associated with this article can be found in the online version at [doi:10.1016/j.apcatb.2022.121420](https://doi.org/10.1016/j.apcatb.2022.121420).

References

- [1] P. Schwach, X. Pan, X. Bao, Direct conversion of methane to value-added chemicals over heterogeneous catalysts: challenges and prospects, *Chem. Rev.* 117 (2017) 8497–8520, <https://doi.org/10.1021/acs.chemrev.6b00715>.
- [2] J.H. Lunsford, Catalytic conversion of methane to more useful chemicals and fuels: a challenge for the 21st century, *Catal. Today* 63 (2000) 165–174, [https://doi.org/10.1016/S0920-5861\(00\)00456-9](https://doi.org/10.1016/S0920-5861(00)00456-9).
- [3] M. Ravi, M. Ranocchiari, J.A. van Bokhoven, The direct catalytic oxidation of methane to methanol—a critical assessment, *Angew. Chem. Int. Ed.* 56 (2017) 16464–16483, <https://doi.org/10.1002/anie.201702550>.
- [4] H. Schwarz, Chemistry of methane: concepts rather than recipes, *Angew. Chem. Int. Ed.* 50 (2011) 10096–10115, <https://doi.org/10.1002/anie.201006424>.
- [5] E. Yang, J.G. Lee, D.H. Kim, Y.S. Jung, J.H. Kwak, E.D. Park, K. An, $\text{SiO}_2/\text{V}_2\text{O}_5/\text{Al}_2\text{O}_3$ core-shell catalysts with high activity and stability for methane oxidation to formaldehyde, *J. Catal.* 368 (2018) 134–144, <https://doi.org/10.1016/j.jcat.2018.09.027>.
- [6] M.R. Smith, U.S. Ozkan, The partial oxidation of methane to formaldehyde: role of different crystal planes of MoO_3 , *J. Catal.* 141 (1993) 124–139, <https://doi.org/10.1006/jcat.1993.1124>.
- [7] J. Tian, J. Tan, Z. Zhang, P. Han, M. Yin, S. Wan, J. Lin, S. Wang, Y. Wang, Direct conversion of methane to formaldehyde and CO on B_2O_3 catalysts, *Nat. Commun.* 11 (2020) 5693, <https://doi.org/10.1038/s41467-020-19517-y>.
- [8] T. Mattisson, A. Lyngfelt, P. Cho, The use of iron oxide as an oxygen carrier in chemical-looping combustion of methane with inherent separation of CO_2 , *Fuel* 80 (2001) 1953–1962, [https://doi.org/10.1016/S0016-2361\(01\)00051-5](https://doi.org/10.1016/S0016-2361(01)00051-5).
- [9] J. Yang, E. Bjørgum, H. Chang, K.-K. Zhu, Z.-J. Sui, X.-G. Zhou, A. Holmen, Y.-A. Zhu, D. Chen, On the ensemble requirement of fully selective chemical looping methane partial oxidation over La-Fe-based perovskites, *Appl. Catal. B* 301 (2022), 120788, <https://doi.org/10.1016/j.apcatb.2021.120788>.
- [10] R. Banerjee, Y. Proshlyakov, J.D. Lipscomb, D.A. Proshlyakov, Structure of the key species in the enzymatic oxidation of methane to methanol, *Nature* 518 (2015) 431–434, <https://doi.org/10.1038/nature14160>.
- [11] A. Matsuda, H. Tateno, K. Kamata, M. Hara, Iron phosphate nanoparticle catalyst for direct oxidation of methane into formaldehyde: effect of surface redox and acid-base properties, *Catal. Sci. Technol.* 11 (2021) 6987–6998, <https://doi.org/10.1039/D1CY01265G>.
- [12] R. Polnišer, M. Štolcová, M. Hronec, M. Mikula, Structure and reactivity of copper iron pyrophosphate catalysts for selective oxidation of methane to formaldehyde and methanol, *Appl. Catal. A* 400 (2011) 122–130, <https://doi.org/10.1016/j.apcata.2011.04.022>.
- [13] Y. Wang, X. Wang, Z. Su, Q. Guo, Q. Tang, Q. Zhang, H. Wan, SBA-15-supported iron phosphate catalyst for partial oxidation of methane to formaldehyde, *Catal. Today* 93 (2004) 155–161, <https://doi.org/10.1016/j.cattod.2004.06.037>.
- [14] X. Wang, Y. Wang, Q. Tang, Q. Guo, Q. Zhang, H. Wan, MCM-41-supported iron phosphate catalyst for partial oxidation of methane to oxygenates with oxygen and nitrous oxide, *J. Catal.* 217 (2003) 457–467, [https://doi.org/10.1016/S0021-9517\(03\)00077-0](https://doi.org/10.1016/S0021-9517(03)00077-0).
- [15] Q. Zhang, Y. Li, D. An, Y. Wang, Catalytic behavior and kinetic features of $\text{FeO}_x/\text{SBA-15}$ catalyst for selective oxidation of methane by oxygen, *Appl. Catal. A* 356 (2009) 103–111, <https://doi.org/10.1016/j.apcata.2008.12.031>.
- [16] J. He, Y. Li, D. An, Q. Zhang, Y. Wang, Selective oxidation of methane to formaldehyde by oxygen over silica-supported iron catalysts, *J. Nat. Gas Chem.* 18 (2009) 288–294, [https://doi.org/10.1016/S1003-9953\(08\)60120-6](https://doi.org/10.1016/S1003-9953(08)60120-6).
- [17] B. Michalkiewicz, Partial oxidation of methane to formaldehyde and methanol using molecular oxygen over Fe-ZSM-5, *Appl. Catal. A* 277 (2004) 147–153, <https://doi.org/10.1016/j.apcata.2004.09.005>.
- [18] K. Shimura, T. Fujitani, Effects of promoters on the performance of a VO_x/SiO_2 catalyst for the oxidation of methane to formaldehyde, *Appl. Catal. A* 577 (2019) 44–51, <https://doi.org/10.1016/j.apcata.2019.03.014>.
- [19] N.D. Spencer, C.J. Pereira, R.K. Grasselli, The effect of sodium on the $\text{MoO}_3/\text{SiO}_2$ -catalyzed partial oxidation of methane, *J. Catal.* 126 (1990) 546–554, [https://doi.org/10.1016/0021-9517\(90\)90019-G](https://doi.org/10.1016/0021-9517(90)90019-G).
- [20] Y. Li, D. An, Q. Zhang, Y. Wang, Copper-catalyzed selective oxidation of methane by oxygen: studies on catalytic behavior and functioning mechanism of $\text{CuO}_x/\text{SBA-15}$, *J. Phys. Chem. C* 112 (2008) 13700–13708, <https://doi.org/10.1021/jp804168y>.
- [21] J.W. Han, C. Kim, J.S. Park, H. Lee, Highly coke-resistant Ni nanoparticle catalysts with minimal sintering in dry reforming of methane, *ChemCatChem* 7 (2014) 451–456, <https://doi.org/10.1002/cssc.201301134>.
- [22] T. Xie, L. Shi, J. Zhang, D. Zhang, Immobilizing Ni nanoparticles to mesoporous silica with size and location control via a polyol-assisted route for coking- and sintering-resistant dry reforming of methane, *Chem. Commun.* 50 (2014) 7250–7253, <https://doi.org/10.1039/C4CC01441C>.
- [23] Y. Dai, B. Lim, Y. Yang, C.M. Cobley, W. Li, E.C. Cho, B. Grayson, P.T. Fanson, C. T. Campbell, Y. Sun, Y. Xia, A sinter-resistant catalytic system based on platinum nanoparticles supported on TiO_2 nanofibers and covered by porous silica, *Angew. Chem. Int. Ed.* 122 (2010) 8341–8344, <https://doi.org/10.1002/anie.201001839>.
- [24] S.H. Joo, J.Y. Park, C.-K. Thung, Y. Yamada, P. Yang, G.A. Somorjai, Thermally stable Pt/mesoporous silica core-shell nanocatalysts for high-temperature reactions, *Nat. Mater.* 8 (2009) 126–131, <https://doi.org/10.1038/nmat2329>.
- [25] S. Lee, J. Seo, W. Jung, Sintering-resistant Pt/ CeO_2 nanoparticles for high-temperature oxidation catalysis, *Nanoscale* 8 (2016) 10219–10228, <https://doi.org/10.1039/C6NR00170J>.
- [26] W.-J. Zhang, Z. Liu, K.-P. Song, C.M. Aikens, S.-S. Zhang, Z. Wang, C.-H. Tung, D. Sun, A 34-electron superatom Ag_{78} cluster with regioselective ternary ligands shells and its 2D rhombic superlattice assembly, *Angew. Chem. Int. Ed.* 60 (2021) 4231–4237, <https://doi.org/10.1002/anie.202013681>.
- [27] K. Zhou, C. Qin, H.-B. Li, L.-K. Yan, X.-L. Wang, G.-G. Shan, Z.-M. Su, C. Xu, X.-L. Wang, Assembly of a luminescent core-shell nanocluster featuring a $\text{Ag}_{34}\text{S}_{26}$ shell and a W_6O_{21} polyoxoanion core, *Chem. Commun.* 48 (2012) 5844–5846, <https://doi.org/10.1039/C2CC32321D>.
- [28] Y. Zhu, H. Qian, R. Jin, An atomic-level strategy for unraveling gold nanocatalysts from the perspective of $\text{Au}_n(\text{SR})_m$ nanoclusters, *Chem. Eur. J.* 16 (2010) 11455–11462, <https://doi.org/10.1002/chem.201001086>.
- [29] M. Sun, J. Zhang, P. Putaj, V. Caps, F. Lefebvre, J. Pelletier, J.-M. Basset, Catalytic oxidation of light alkanes (C_1 – C_4) by heteropoly compounds, *Chem. Rev.* 114 (2014) 981–1019, <https://doi.org/10.1021/cr300302b>.
- [30] S.-S. Wang, G.-Y. Yang, Recent advances in polyoxometalate-catalyzed reactions, *Chem. Rev.* 115 (2015) 4893–4962, <https://doi.org/10.1021/cr500390v>.
- [31] P. Putaj, F. Lefebvre, Polyoxometalates containing late transition and noble metal atoms, *Coord. Chem. Rev.* 255 (2011) 1642–1685, <https://doi.org/10.1016/j.ccr.2011.01.030>.
- [32] D.-L. Long, R. Tsunashima, L. Cronin, Polyoxometalates: building blocks for functional nanoscale systems, *Angew. Chem. Int. Ed.* 49 (2010) 1736–1758, <https://doi.org/10.1002/anie.200902483>.

- [33] A. Téazéa, G. Hervéa, R.G. Finke, D.K. Lyon, α -, β -, and γ -Dodecatungstosilicic acids: isomers and related lacunary compounds, *Inorg. Synth.* 27 (1990) 85–96, <https://doi.org/10.1002/9780470132586.ch16>.
- [34] K. Suzuki, M. Shinoue, N. Mizuno, Synthesis and reversible transformation of Cu_n -bridged ($n = 1, 2$, or 4) silicododecatungstate dimers, *Inorg. Chem.* 51 (2012) 11574–11581, <https://doi.org/10.1021/ic301488a>.
- [35] K. Suzuki, F. Tang, Y. Kikukawa, K. Yamaguchi, N. Mizuno, Visible-light-induced photoredox catalysis with a tetracerium-containing silicododecatungstate, *Angew. Chem. Int. Ed.* 53 (2014) 5356–5360, <https://doi.org/10.1002/anie.201403215>.
- [36] K. Suzuki, R. Sato, T. Minato, M. Shinoue, K. Yamaguchi, N. Mizuno, A cascade approach to hetero-pentamuclear manganese-oxide clusters in polyoxometalates and their single-molecule magnet properties, *Dalton Trans.* 44 (2015) 14220–14226, <https://doi.org/10.1039/C5DT01363A>.
- [37] Y. Kikukawa, Y. Kuroda, K. Suzuki, M. Hibino, K. Yamaguchi, N. Mizuno, A discrete octahedrally shaped $[\text{Ag}_6]^{4+}$ cluster encapsulated within silicododecatungstate ligands, *Chem. Commun.* 49 (2013) 376–378, <https://doi.org/10.1039/C2CC37591E>.
- [38] S. Pei, B. Yue, L. Qian, S. Yan, J. Cheng, Y. Zhou, S. Xie, H. He, Preparation and characterization of P–Mo–V mixed oxide-incorporating mesoporous silica catalysts for selective oxidation of methane to formaldehyde, *Appl. Catal. A* 329 (2007) 148–155, <https://doi.org/10.1016/j.apcata.2007.07.008>.
- [39] O. Benlounes, S. Mansouri, C. Rabia, S. Hocine, Direct oxidation of methane to oxygenates over heteropolyanions, *J. Nat. Gas Chem.* 17 (2008) 309–312, [https://doi.org/10.1016/S1003-9953\(08\)60070-5](https://doi.org/10.1016/S1003-9953(08)60070-5).
- [40] S. Mansouri, O. Benlounes, C. Rabia, R. Thouvenot, M.M. Bettahar, S. Hocine, Partial oxidation of methane over modified Keggin-type polyoxotungstates, *J. Mol. Catal. A Chem.* 379 (2013) 255–262, <https://doi.org/10.1016/j.molcata.2013.08.006>.
- [41] A. Bielański, A. Malecka-Lubańska, A. Micek-Ilnicka, J. Poźniczek, The role of protons in acid–base type reactions on heteropolyacid catalysts: gas-phase MTBE synthesis on $\text{H}_4\text{SiW}_{12}\text{O}_{40}$, *Top. Catal.* 11 (2000) 43–53, <https://doi.org/10.1023/A:1027252015190>.
- [42] Yarnton, O.D. Rigaku, CrysAlis PRO, Rigaku Oxford Diffraction Ltd, England, 2018.
- [43] G.M. Sheldrick, A short history of SHELX, *Acta Crystallogr. A* 64 (2008) 112–122, <https://doi.org/10.1107/S0108767307043930>.
- [44] G.M. Sheldrick, Crystal structure refinement with SHELXL, *Acta Crystallogr. C* 71 (2015) 3–8, <https://doi.org/10.1107/S2053229614024218>.
- [45] P. van der Sluis, A.L. Spek, BYPASS: An effective method for the refinement of crystal structures containing disordered solvent regions, *Acta Crystallogr. A* 46 (1990) 194–201, <https://doi.org/10.1107/S0108767389011189>.
- [46] K. Kamata, K. Yonehara, Y. Sumida, K. Yamaguchi, S. Hikichi, N. Mizuno, Efficient epoxidation of olefins with $\geq 99\%$ selectivity and use of hydrogen peroxide, *Science* 300 (2003) 964–966, <https://doi.org/10.1126/science.1083176>.
- [47] K. Kamata, M. Kotani, K. Yamaguchi, S. Hikichi, N. Mizuno, Olefin epoxidation with hydrogen peroxide catalyzed by lacunary polyoxometalate $[\gamma\text{-SiW}_{10}\text{O}_{34}(\text{H}_2\text{O})_2]^{4-}$, *Chem. Eur. J.* 13 (2007) 639–648, <https://doi.org/10.1002/chem.200600384>.
- [48] K. Otsuka, Y. Wang, I. Yamanaka, A. Morikawa, Kinetics study of the partial oxidation of methane over $\text{Fe}_2(\text{MoO}_4)_3$ catalyst, *J. Chem. Soc. Faraday Trans.* 89 (1993) 4225–4230, <https://doi.org/10.1039/FT9938904225>.
- [49] J.-J. Tang, B. Liu, Reactivity of the $\text{Fe}_2\text{O}_3(0001)$ surface for methane oxidation: a GGA + U study, *J. Phys. Chem. C* 120 (2016) 6642–6650, <https://doi.org/10.1021/acs.jpcc.6b00374>.
- [50] S. Kasztelan, J.B. Moffat, The oxidation of methane on heteropolyoxometalates: I. Catalytic properties of silica-supported heteropolyacids, *J. Catal.* 106 (1987) 512–524, [https://doi.org/10.1016/0021-9517\(87\)90264-8](https://doi.org/10.1016/0021-9517(87)90264-8).
- [51] M. Tang, L. Xu, M. Fan, Progress in oxygen carrier development of methane-based chemical-looping reforming: a review, *Appl. Energy* 151 (2015) 143–156, <https://doi.org/10.1016/j.apenergy.2015.04.017>.
- [52] T.E. Westre, P. Kennepohl, J.G. DeWitt, B. Hedman, K.O. Hodgson, E.I. Solomon, A multiplet analysis of Fe K-edge $1s \rightarrow 3d$ pre-edge features of iron complexes, *J. Am. Chem. Soc.* 119 (1997) 6297–6314, <https://doi.org/10.1021/ja964352a>.
- [53] Z. Yang, S. Zhang, H. Zhao, A. Li, L. Luo, L. Guo, Subnano- FeO_x clusters anchored in an ultrathin amorphous Al_2O_3 nanosheet for styrene epoxidation, *ACS Catal.* 11 (2021) 11542–11550, <https://doi.org/10.1021/acscatal.1c01366>.